

Sub-micron particle organization by self-imaging of non-diffracting beams

This content has been downloaded from IOPscience. Please scroll down to see the full text.

2006 New J. Phys. 8 43

(<http://iopscience.iop.org/1367-2630/8/3/043>)

View [the table of contents for this issue](#), or go to the [journal homepage](#) for more

Download details:

IP Address: 128.122.52.180

This content was downloaded on 02/06/2014 at 17:21

Please note that [terms and conditions apply](#).

Sub-micron particle organization by self-imaging of non-diffracting beams

Tomáš Čižmár¹, Věra Kollárová², Zdeněk Bouchal²
and Pavel Zemánek¹

¹ Institute of Scientific Instruments, Academy of Sciences of the Czech Republic, Královopolská 147, 612 64 Brno, Czech Republic

² Department of Optics, Palacky University, 17. listopadu 50, 772 07 Olomouc, Czech Republic

E-mail: pavlik@isibrno.cz

New Journal of Physics **8** (2006) 43

Received 6 January 2006

Published 24 March 2006

Online at <http://www.njp.org/>

doi:10.1088/1367-2630/8/3/043

Abstract. We present the first theoretical and experimental study of dielectric sub-micron particle behaviour in an optical field generated by interference of co-propagating non-diffracting beams of different propagation constants. In such a field, there are periodic oscillations of the on-axial intensity maxima (self-imaging) that are frequently mentioned as useful for optical trapping. We show that in three dimensions this is true only for very small particles and the increasing number of interfering beams does not enable confinement of substantially bigger particles under the studied conditions. Experimentally, we succeeded in optical confinement of beads radii from 100 nm up to 300 nm but only with the help of fluid flow against the beams propagation. We observed self-organization of the particles into the periodic 1D array with the interparticle distance equal to $7.68\ \mu\text{m}$. We observed how a bead jump from one trap to the neighbouring-occupied trap caused a domino effect propagating with constant velocity over the subsequent occupied traps. Phase shift in one beam induced controlled bi-directional shift of the whole structure over a maximal distance of $250\ \mu\text{m}$ in two co-propagating Bessel beams.

Contents

1. Introduction	2
2. Theoretical analyses of particle behaviour in two co-propagating BBs	3
3. Experimental setup	8
4. Experimental results	10
5. More co-propagating BBs	13
6. Conclusions	16
Acknowledgments	17
Appendix A. Calculation of optical forces in BBs	17
References	21

1. Introduction

Specially prepared optical fields can be efficiently used to suppress the thermal motion of micron-size and even sub-micron-size objects and spatially localized single or more particles in periodic structures. Once the objects are localized they can be optically reconfigured, delivered in space or even sorted according to their properties. These mechanisms are very useful in fluid systems where biological micro-objects or colloidal objects are studied. In this paper co-propagating interfering non-diffracting beams of two different micron-size core widths are used for optical localization of sub-micron objects and their bi-directional delivery, their spatial organization into one-dimensional (1D) array and study of their Brownian motion.

A monochromatic non-diffracting beam was introduced as a special solution of the Helmholtz equation whose temporally independent complex amplitude has a mode-like form $\mathbf{E}(x, y, z) = \mathbf{E}_{B0}(x, y; k_r) \exp(-ik_z z)$, where k_r and k_z are related to the wave number k as $k_r^2 = k^2 - k_z^2$. During propagation along the z -coordinate, the field exhibits phase oscillations given by the propagation constant k_z but its longitudinal component of the Poynting vector S_z (see appendix equation (A.12)) remains unchanged. In the first work on scalar non-diffracting beams [1], the amplitude E_{B0} was obtained in the form of the Bessel function. Nowadays, a broad class of these beams is known, from the most simple scalar Bessel beams (BBs) [1] and Mathieu beams [2] to vectorial descriptions, optical vortices, and generalized propagation-invariant wave fields [3]–[5]. The amplitude of the non-diffracting beam is not restricted to a form given by the known mathematical functions. In the integral treatment, an infinite number of beams with different intensity profiles including various patterns and beam arrays can be designed and realized. In advanced experiments, a transverse intensity profile of the non-diffracting field can even be shaped to a predetermined form. Very promising effects appear if two or more co-directional non-diffracting beams interfere. If their propagation constants are properly chosen, the non-diffracting beams exhibit constructive and destructive interference at the distances repeating with the period z_T —historically known as ‘Talbot distance’ [6]. As a consequence, the longitudinal component of the Poynting vector exhibits a longitudinal periodicity known as the self-imaging, $S_z(x, y, z) = S_z(x, y, z + z_T)$. This effect was first analysed and measured in 1996 [7] for two beams, later on it was studied in more details and worked out for more beams including rotating ones [8]–[11]. For two interfering beams, the total field has a cosine longitudinal evolution but

for more beams strong intensity peaks appearing periodically along the propagation direction can be observed (see appendix, figure A.1).

Since non-diffracting beams form an orthogonal base, it was suggested how to form the required longitudinal intensity profile [12] too. BBs were employed in several interesting trapping experiments—simultaneous manipulation in several sample cells using single BB [13], microparticle guiding in arrays of BBs generated by manufactured micro-axicons [14], three micron-size silica spheres self-arrangement in vertical BB [15], and optical conveyor belt based on counter-propagating and interfering BBs [16]. Except the last one, all of them used wide beams with core diameters in tens of micrometres.

Several other publications also dealt with the interference of Gaussian, Laguerre–Gaussian or BBs of different widths but they were more focused on the design of ‘bottle beams’—beams with intensity minimum surrounded by intensity maximum [17]–[23] or braided nodal lines in wave superposition [24]. The majority of them mentioned optical tweezers and optical trapping as one of the possible fields of applications because such a beam enables spatial confinement of micro-objects having a lower refractive index compared to the surrounding medium or atoms into blue-detuned dipole trap. The Talbot effect has been recently used for the generation of 3D interferometric tweezers, too [25].

In contrast to the majority of the above-mentioned examples, we present here the use of self-imaging for optical 3D confinement of one order smaller particles (sub-micron ones) with higher refractive index compared to the surrounding medium. In this case, the longitudinal intensity changes give rise to a gradient optical force pushing the object to an on-axis intensity maximum. At the same time the scattering force (radiation pressure) coming from both co-propagating beams pushes the particles in the direction of both beams. To confine a particle of radius a , the longitudinal component of the gradient force has to balance the scattering force and therefore, the longitudinal oscillation of the field (Talbot distance [6]) has to be as short as possible³. Since the scattering force rises as a^6 and the gradient one as a^3 , the equilibrium can be achieved only for smaller particles.

2. Theoretical analyses of particle behaviour in two co-propagating BBs

The theoretical analyses are based on our model describing the ideal non-paraxial BB behind the axicon. Because of unique symmetries of this beam, the optical forces can be expressed without tedious double integrations [26]. We discuss this model in detail in the appendix. Based on this model, we compromised the widths of the BB cores with respect to the Talbot distance, available laser power and properties of optical components. Figure 1 shows the longitudinal profile of the optical force for various radii of polystyrene spheres placed in a water medium. It is seen that bigger objects are indeed pushed away from the on-axial intensity maximum (placed at $z = 0$ here) towards the intensity minimum until the gradient force is not able to compensate the scattering force. Surprisingly, the axial depth of the optical trap dW_z increases with growing sphere size until its global maximum, behind which it steeply decreases to zero (see figure 2). The length of the trap L_z (defined in figure 1) steeply decreases as the equilibrium position moves away from intensity maximum and gradually it reaches a sort of steady value close to $1\ \mu\text{m}$

³ Even though the terms ‘gradient’ and ‘scattering’ forces are valid only in connection with very small objects (point dipoles or Rayleigh particles), we used them here even for slightly bigger sub-micron size objects. We believe that this terminology explains the problem more lucidly without severe incorrectness.

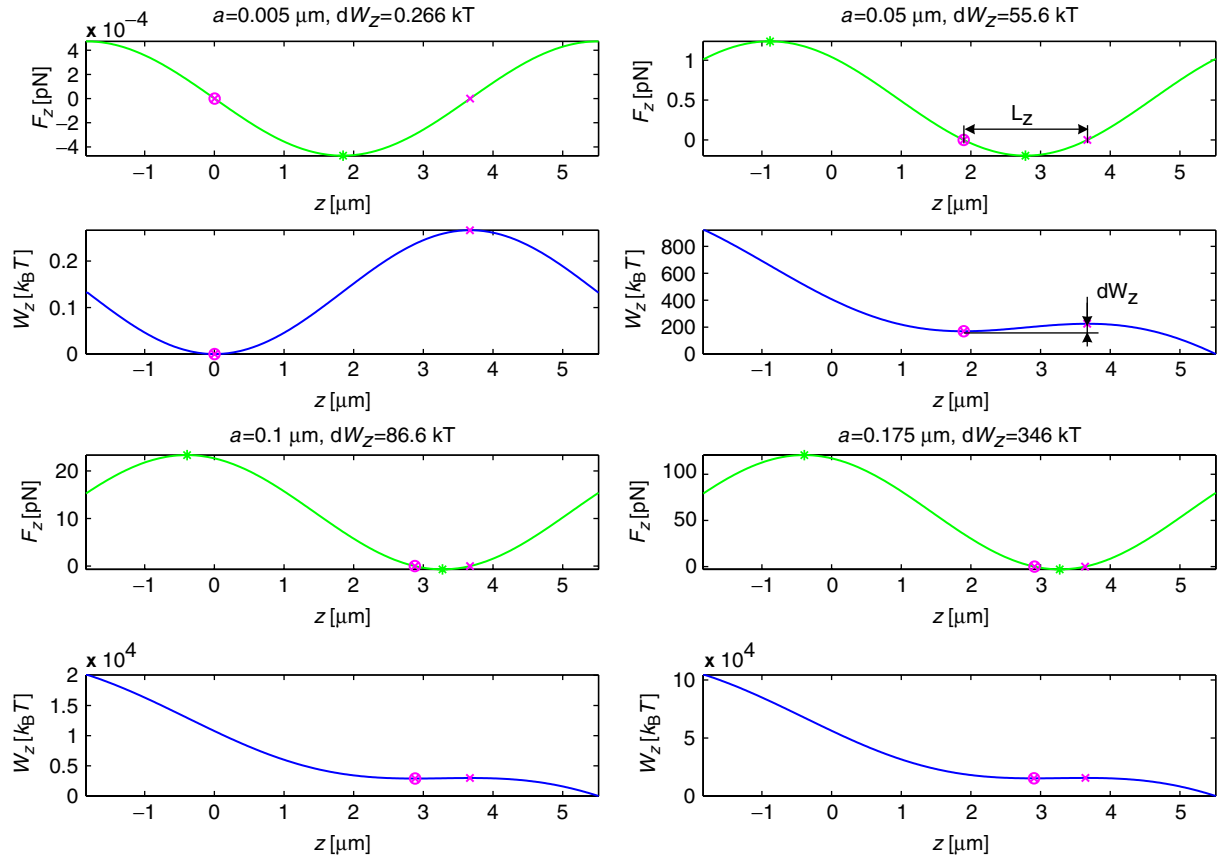


Figure 1. Simulations of the optical longitudinal force (green lines) at the centre of both co-propagating BBs of core radii $r_{\text{bes}1} = 0.437 \mu\text{m}$, $r_{\text{bes}2} = 1.156 \mu\text{m}$ for four radii of polystyrene spheres $a = 0.005, 0.05, 0.1$ and $0.175 \mu\text{m}$. Talbot distance (longitudinal spatial period of F_z) is equal to $z_{\text{Tth}} = 7.34 \mu\text{m}$. r_{bes} and z_{T} are defined in equations (A.13) and (A.19). The equilibrium position is labelled by \otimes , non-equilibrium position by \times and forces extrema by $*$. The blue lines show the axial potential profile done by $W_z = -\int F_z dz$. For the purpose of further analyses, we define trap depth dW_z and trap length L_z as explained in the top right plots. We assumed the intensity of the electric field on the optical axis as the same for both beams and it was equal to the electric field intensity of a 1 W Gaussian beam with beam waist $1 \mu\text{m}$ ($E = 1.8 \times 10^{12} \text{ V m}^{-1}$).

(see figure 2). From figure 2 we see that there exists an optimal sphere size for which the selected beam configuration provides the deepest optical trap axially. The bigger the difference in the radii between both beams used, the shorter the Talbot distance, consequently the stronger the gradient force and bigger objects can be confined. However, the laser provides only finite output power that has to be non-equally split between both beams. The wider beam carries more power because the electric field intensity on optical axis has to be the same for both beams to obtain destructive interference reaching zero value. If we assume that the trap depth sufficient for object confinement is equal to $10k_{\text{B}}T$, laser power $\simeq 65 \times$ smaller is needed comparing to the values $P_{\text{bes}1}$ and $P_{\text{bes}2}$ used for our simulations shown in figure 2. This is an experimentally achievable value.

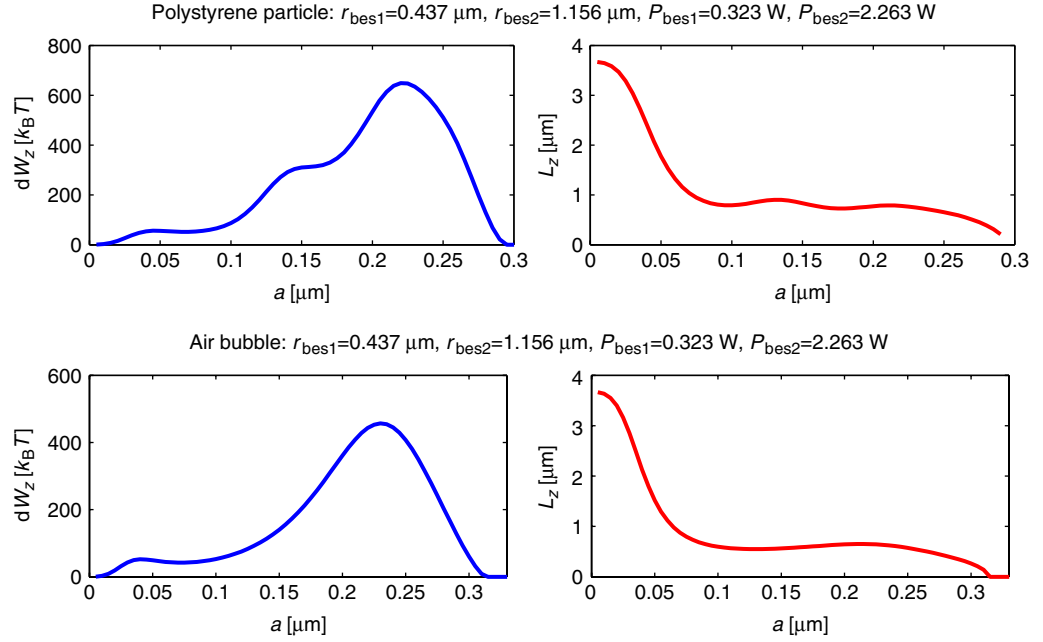


Figure 2. The axial depth of the optical trap dW_z and axial length of the trap L_z for different radii of polystyrene spheres (top plots, see [movie 1](#)) and air bubbles (bottom plots, see [movie 2](#)) dispersed in water. The radii of the BB cores and the on-axis electric field intensities were the same as in figure 1. This gives the necessary powers in the central core of the BBs P_{bes1} and P_{bes2} (see equation (A.15)). It is seen that sphere radii bigger than $0.3 \mu\text{m}$ cannot be confined by optical forces only. On the other hand, there exists an optimal particle radius that provides the deepest trap ($a \simeq 0.22 \mu\text{m}$, in this case, gives $dW_z \simeq 650k_B T$).

As the equilibrium position moves away from the intensity maximum with increasing sphere size, the radial forces localizing the object on the optical axis are getting weaker. Finally the object can escape in radial direction. The overview of the particle behaviour in x - z -plane is shown in figure 3 for the same radius ($a = 205 \text{ nm}$) of polystyrene bead and air bubble. The pink curves show the trajectories of the particle if started at various places in the plane. The grey ellipse represents the object size (radius $a = 205 \text{ nm}$) in proportion to the axis scales placed at one selected equilibrium position (optical trap).

Despite the fact that the system is not conservative and so the work generally depends on the object trajectory, we at least estimated how much work is needed to free the object radially from the selected trap. We started at the equilibrium position and pushed the object radially from the trap against the optical force till the sign of the work increment $F_x dx + F_z dz$ changed. The lengths of these trajectories are shown in figure 4 as pink lines. It is seen that for polystyrene beads (left column) the length of these lines is minimal for certain off-axis angles. This is accompanied by the work minimum (for $a = 205 \text{ nm}$ bead) or even release of the object from the trap ($a = 260 \text{ nm}$) as is shown in the $dW(\alpha)$ plots placed below the odd lines of figures. Even though we found from the axial analyses that the polystyrene bead of radius $a = 260 \text{ nm}$ is confined axially, it will escape radially for polar angles in the range 34 – 150° . Generally speaking the

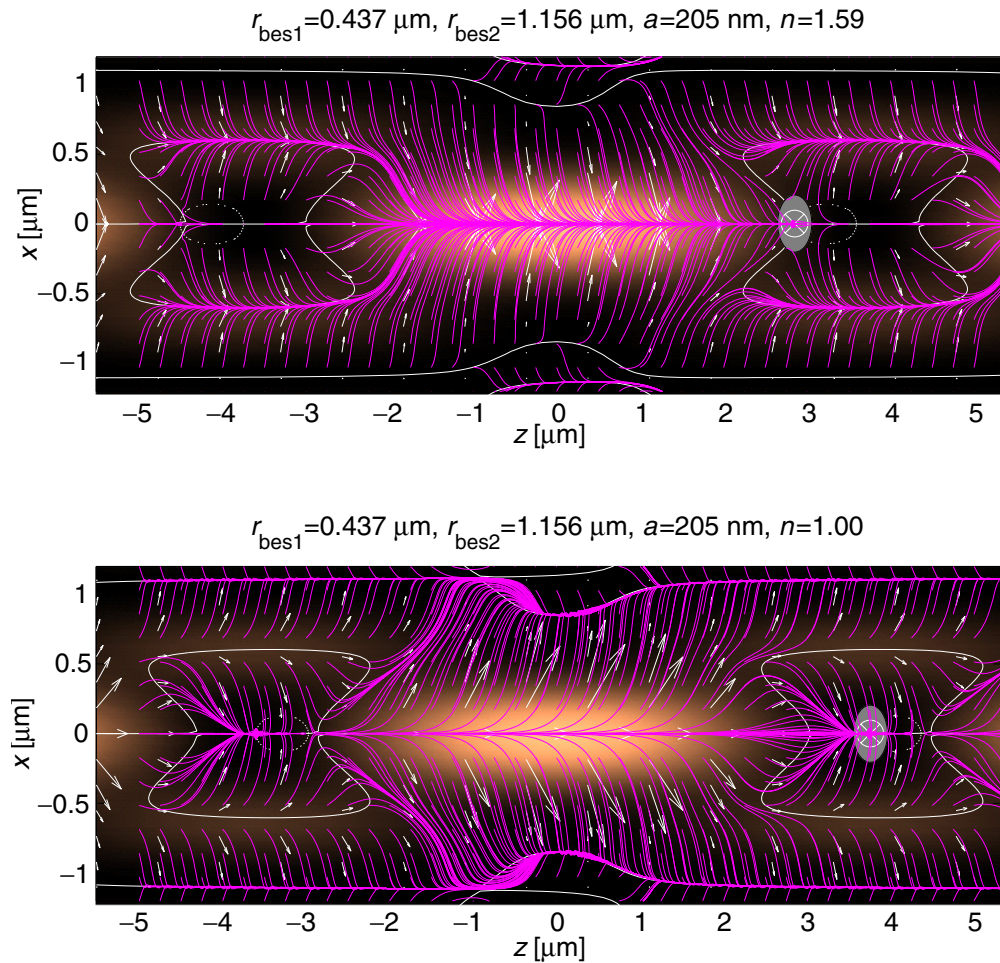


Figure 3. The side view of the optical intensity of the two co-propagating BBs. The lighter regions correspond to the higher intensity. The dark regions on both sides of the intensity maximum are surrounded by the lighter regions of higher intensity forming an ‘optical bottle’. White arrows show the optical forces acting on a polystyrene particle (top image) and air bubble (bottom image) of radius 205 nm. The pink curves show the object trajectories if the object starts at different places of the figure. The grey ellipse represents the object size (radius $a = 205 \text{ nm}$) in proportion to the axis scales placed at one selected equilibrium position (optical trap) denoted by \otimes . The white full and dotted curves denote the places where $F_r = 0$ and $F_z = 0$, respectively. It is clearly seen that if a polystyrene particle is placed off-axis inside the optical bottle, it is pushed radially away from the optical axis to the places of the higher intensity. From these places, it is gradually pushed back to the central intensity maximum, passes through it and is settled in neighbouring optical trap. In contrast, the air bubble is settled at the intensity minimum and so its position is less sensitive to its increase in the size. But only the objects appearing in the proximity of the intensity minimum are pushed into this trap. All the other objects are pushed off-axis into the intensity minimum between the lateral fringes where they are propelled in the direction of both beams.

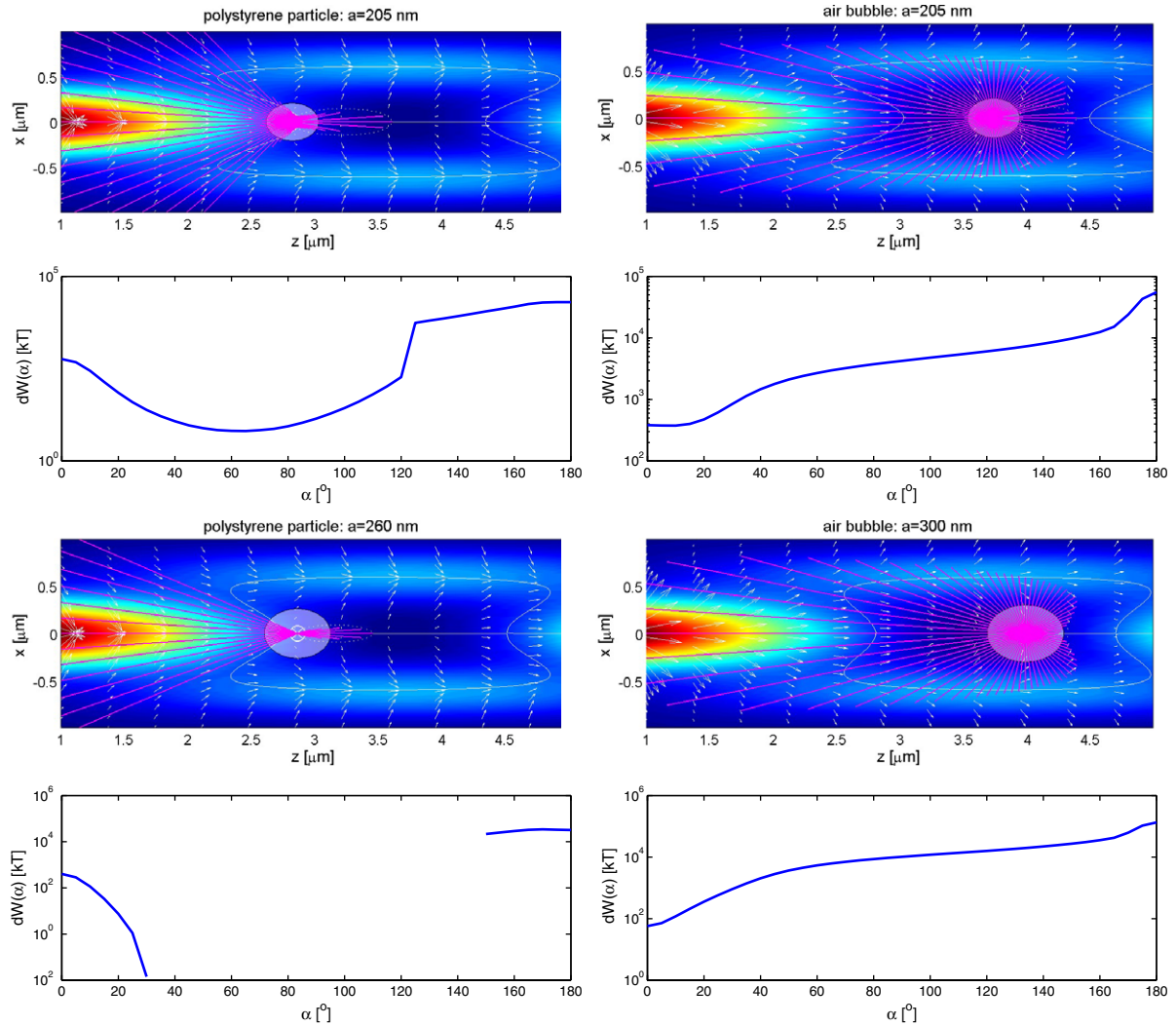


Figure 4. Analyses of the radial properties of optical traps created in two co-propagating BBs having core radii $r_{\text{bes1}} = 0.437 \mu\text{m}$, $r_{\text{bes2}} = 1.156 \mu\text{m}$ and the same parameters as in the previous figures. The dark blue regions of intensity minimum are surrounded by regions of higher intensity forming an ‘optical bottle’. White arrows show the optical forces acting on the selected particle radii (left column, polystyrene beads; right column, air bubbles). The pink lines show the radial trajectories along which we calculated the work needed to free the object from the selected trap. The obtained values of the work are shown in the plots below in logarithmic y scale. The grey ellipse represents the object placed at the equilibrium position denoted by \otimes . The white full and dotted curves denote the places where $F_r = 0$ and $F_z = 0$, respectively.

work needed to free the polystyrene particle in certain angles radially can be by several orders smaller than it was found in figure 2. In contrast even bigger air bubbles ($a = 300 \text{ nm}$) stay confined. It can be roughly said that the work minimum (see the right column in figure 4) is along the axial axis and its value corresponds to the values mentioned in figure 2.

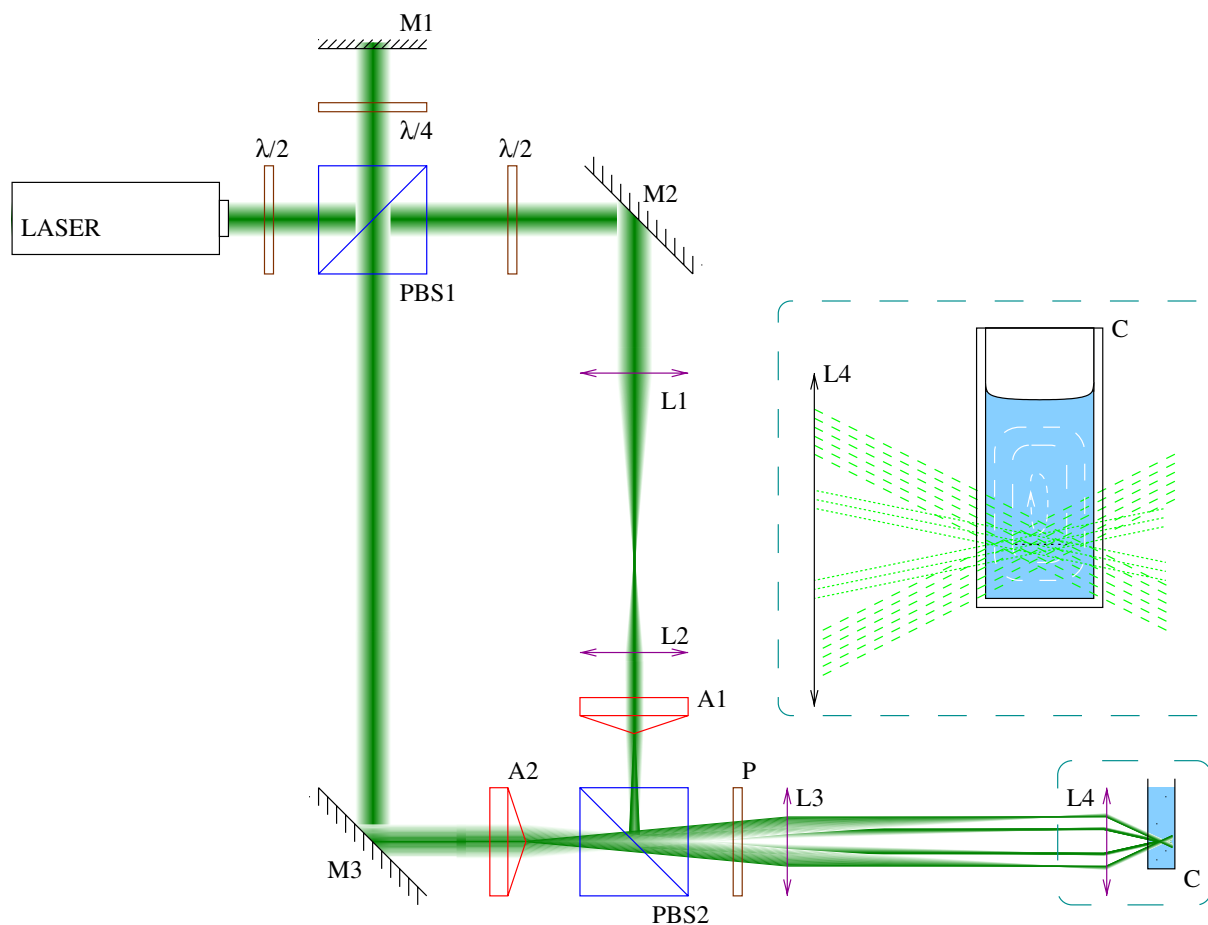


Figure 5. Experimental setup. M_1 – M_3 , mirrors; $\lambda/2$, $\lambda/4$, wave plates; $PBS_{1,2}$, polarizing beam splitters; L_1 – L_4 , lenses; A_1 , A_2 , axicons; P , polarizer; C , cuvette filled with water. The inset shows the water circulation caused by laser heating.

All these results just indicate the properties of the trapping configuration and help us to understand the behaviour of the objects intuitively. More appropriate theoretical treatment should use the stochastic simulations and analyses of the objects' mean first passage time [27, 28].

3. Experimental setup

The experimental setup is shown in figure 5. We used a Verdi V5 (Coherent) laser having vacuum wavelength 532 nm and maximal power 5.5 W. The beam passes through a $\lambda/2$ wave plate tuning their linear polarization so that the powers in both beams obtained behind PBS_1 can be set properly to get destructive interference on the optical axis behind L_4 . The first beam is reflected by PBS_1 , its polarization is changed to circular passing through $\lambda/4$, its direction is reversed on mirror M_1 and its polarization is again turned to linear passing again through $\lambda/4$. Axial motion of mirror M_1 changes the phase of this wave. Since now the polarization is rotated by 90° with respect to the original one, the beam passes through the PBS_1 , reflects on M_3 and passes through an axicon A_2 (Eksma 130-0260, apex angle equal to 160°). Behind A_2 , a BB is

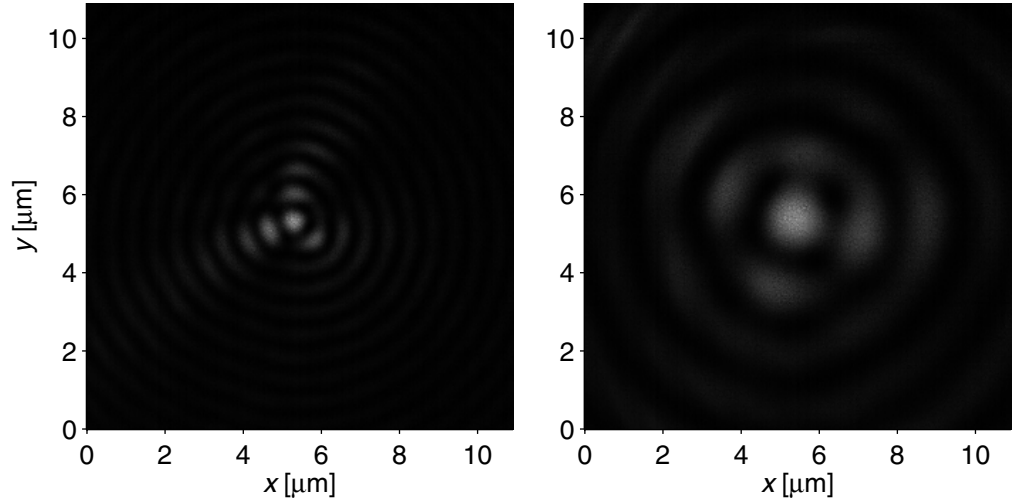


Figure 6. Lateral intensity profiles of the BBs taken behind L4 without the cuvette. A2 formed the narrower beam (left) and A1 the wider beam (right).

formed with the core diameter equal to $4.9 \mu\text{m}$. The second beam behind PBS1 passes through a $\lambda/2$ plate changing its linear polarization by 90° and reflects on M2. Its width is decreased $2\times$ by a telescope made from lenses L1, L2 and the beam passes through A1 (Eksma 130-0270, apex angle equal to 170°). The BB is formed with a core diameter equal to $9.2 \mu\text{m}$. Both beams are merged together by PBS2 and their widths are decreased $5\times$ by a telescope consisting of lenses L3 and L4 with focal lengths 40 and 8 mm, respectively. The apexes of both axicons are placed at the focal plane of L3 to get the axial overlap of the regions where both BBs exist. Since the width of the second beam is decreased $2\times$, these regions are of about the same length for both beams. The polarizations of both beams behind the PBS2 are perpendicular and therefore the polarizer P is rotated by 45° to get interference of both beams. Unfortunately, half of the trapping power is wasted here.

If the cuvette C was missing, each of the beams was imaged on the calibrated CCD (see figure 6). The narrower beam suffered by threefold aberrations and the bigger beam by weaker fourfold aberrations. These aberrations were primarily caused by the quality of the used axicons because the pattern followed rotation of the axicons. By fitting the optical intensity at the detector (see appendix equation (A.12)) to the data from these figures, we found that the radius of the central high-intensity ring is equal to $0.437 \pm 0.001 \mu\text{m}$ for narrower beam and $1.156 \pm 0.003 \mu\text{m}$ for wider beam. It gives the theoretical period of self-imaging along the propagation axis equal to $z_{\text{Th}} = 7.34 \mu\text{m}$ (equation (A.19)) in water. These values were used in the calculation of optical forces and trap depths presented in figures 1 and 2. Figure 7 shows the interference of both beams screened at different positions along the z -axis. The destructive interference at the centre of the beams is clearly visible.

When we studied the sub-micron particle behaviour, the cuvette C was filled by water and placed into the setup. The light scattered by these objects was imaged on a CCD camera placed perpendicularly to the beam. The laser beams generated thermal water circulation in the cuvette; its velocity was bigger for higher water level. The fluid velocity was estimated from the velocity of the untrapped but visible objects passing through the confined objects.

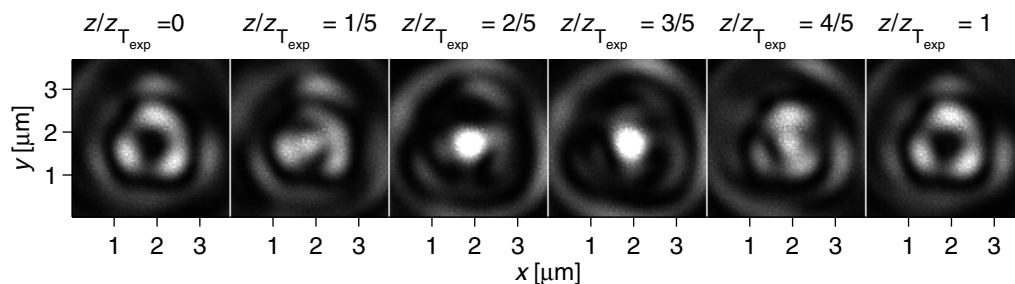


Figure 7. Interference of both co-propagating BBs behind L4 taken by phase shifting of the first beam on the mirror M1 in the configuration without cuvette C. One period (Talbot distance) is shown.

4. Experimental results

We were interested in how many objects we were able to trap with our setup, how big they were, how far from each other they settled and how observed behaviour coincided with our expectations. We used a cuvette filled with water and the height of the water level inside the cuvette determines the thermal water motion caused by the laser beams. Unfortunately with no fluid flow we were not able to force the tested particles of radii $a = 100, 175, 205, 260$ and 300 nm to stay in the optical trap long enough to prove they are trapped. All particles followed the direction of both beams but after a distance smaller than the Talbot one they left the beam centre and departed laterally. Even though both beams interfered destructively on the optical axis (see figure 7), the optical trap in the longitudinal direction was not deep enough to keep the particle trapped for observation time. The main reason was power losses in the optical path and low output power of the used laser (5.5 W).

To overcome this problem, we increased the amount of water inside the cuvette and weak thermal water circulation was generated by the laser. In this case, we were able to compensate the scattering force and to confine the objects near the on-axial intensity maxima. An array of organized polystyrene objects of all studied sizes was obtained (see figure 8).

When the objects were organized into 1D array so that several neighbouring longitudinal optical traps were occupied, we observed how an object left its trap and forced its neighbour to empty its trap (see figure 9). This ‘excitement’ repeatedly propagated along the 1D beads array. In contrast to the observed ‘breathing mode’ in optically bound matter [29], we have not seen the movement of the whole structure. From CCD records, we analysed the beads motion by particle tracking correlation algorithm [30] and the results are presented in figure 10. The left panel of figure 10 shows the histograms of longitudinal particle positions that were used to find the boundaries between the neighbouring traps. Around each maximum, we fitted one period of expected sinusoidal dependence $a \cdot \exp(-b \cdot \sin(x - x_0)^2)/k_B \cdot T$. Where the fitted parameters were a, b, x_0 and k_B is the Boltzmann constant and T the absolute temperature. We found the minimum between each neighbouring maxima and we set this minimum as the boundary between neighbouring traps. These boundaries are represented as \otimes in the right panel of figure 10. When the object crosses over this boundary, it is considered as a jump to the neighbouring trap. We used the same slope and connected the subsequent jumps by dotted lines. This single slope follows very well the jump events in seven subsequent

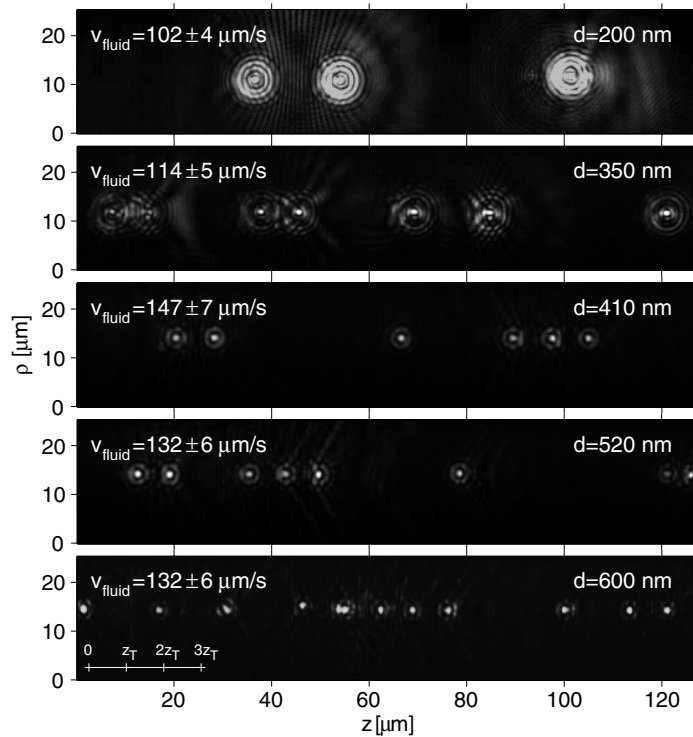


Figure 8. Examples of several objects of different sizes confined in two co-propagating and interfering BBs. Weak water flow against the beam propagation was generated by laser heating of the fluid. It pushed the objects closer to the on-axial intensity maxima so that they were better confined laterally.

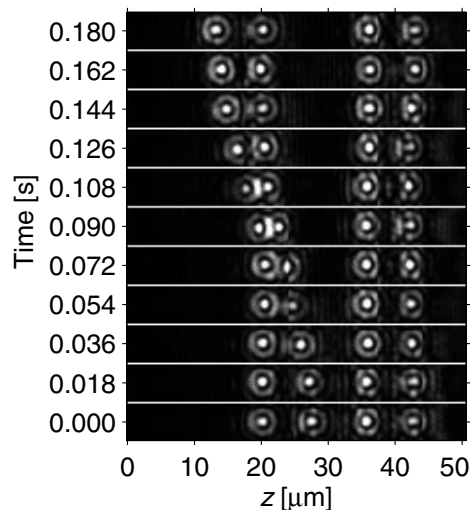


Figure 9. Visual example of the jump of the second bead (from the left) to its neighbour trap occupied by another bead. The jump of the bead from one trap to the other takes an average of 0.0123 ± 0.0016 s. The diameter of the polystyrene beads was equal to 520 nm. (See [movie 3](#).)

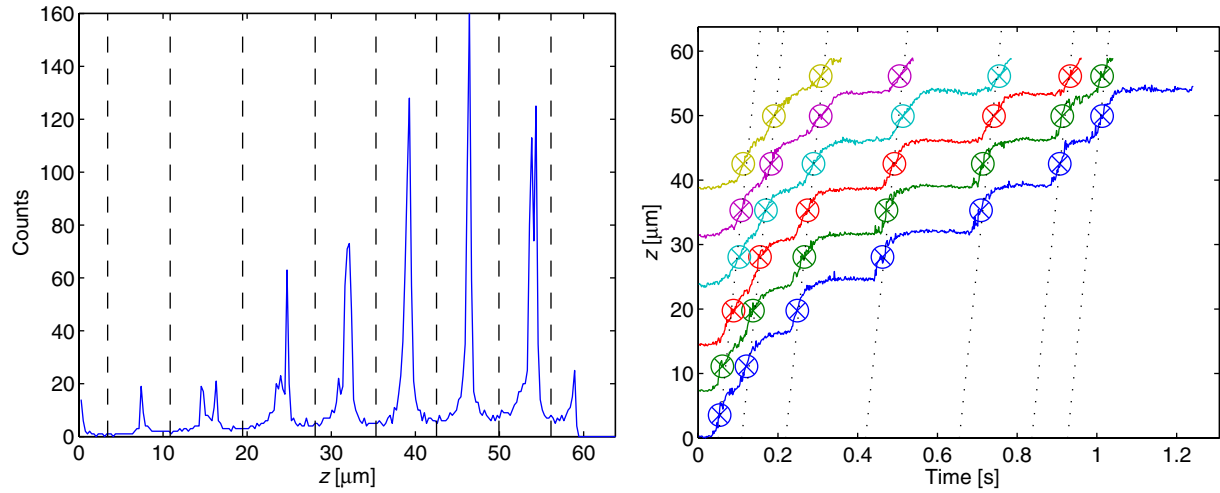


Figure 10. Left panel: histogram of the longitudinal bead positions of a record with six objects (full blue curve). The average distance between neighbouring longitudinal equilibrium beads positions is $z_{\text{Texp}} = 7.68 \mu\text{m}$. This ‘measured’ Talbot distance coincides very well with the ‘theoretical’ one found above from the radii of the BBs $z_{\text{Tth}} = 7.34 \mu\text{m}$. The dashed lines show the boundaries between neighbouring traps (see the text for how they were found). The radius of this polystyrene beads was equal to 300 nm. Right panel: full curves show the time record of the longitudinal position of each polystyrene bead (radius equal to 300 nm) in different colours. \otimes denotes the moments when the beads cross the boundaries between neighbouring traps. Dotted lines connect these moments using the same slope for all jumps. The velocity of the excitement spreading over this 1D array is equal to $620 \pm 80 \mu\text{m s}^{-1}$.

excitements and gives the velocity of the excitement propagation equal to $620 \pm 80 \mu\text{m s}^{-1}$ for the studied particles.

Since our setup enables us to change the phase in one beam with respect to the other, we shifted longitudinally the whole structure of intensity maxima and minima. If the optical traps are occupied, the confined objects can be delivered in this way over a region where both BBs overlapped (see figure 11 for polystyrene beads of diameter 520 nm). This mechanism is similar to that used for optical conveyor belt [16] but here the co-propagating beams are used instead of counter-propagating ones.

The distance between neighbouring optical traps is bigger in the co-propagating beams comparing to the counter-propagating ones. Therefore, the self-reconstructing property of BBs [31, 32] restores the original BB profile at the location of the next trapped object for the object diameters used in the experiments. Figure 12 demonstrates side view on the ideal BB without any object (left image, $a = 0 \text{ nm}$), with the biggest object used in our experiments (middle, $a = 300 \text{ nm}$) and with a polystyrene sphere with radius $a = 3 \mu\text{m}$ (right). It is seen that for $d = 3 \mu\text{m}$ the beam is severely disturbed at the place of the Talbot distance. In contrast, for particle radius $a = 300 \text{ nm}$, the BB restores its intensity profile at the measured Talbot distance $z_{\text{Texp}} = 7.68 \mu\text{m}$ and it ensures very similar trapping conditions for all confined objects. These figures were obtained using the scalar free-space propagation method [33].

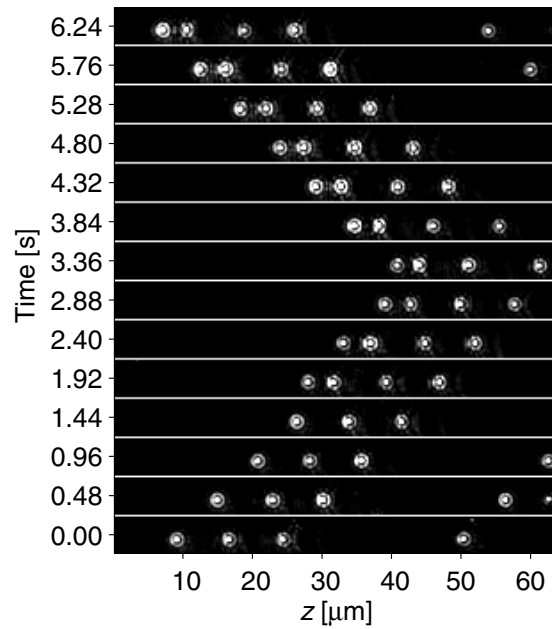


Figure 11. An example of the delivery of five polystyrene beads of diameter 520 nm over a distance of $40\text{ }\mu\text{m}$ by changing the phase of one of the co-propagating BBs. (See [movie 4](#).)

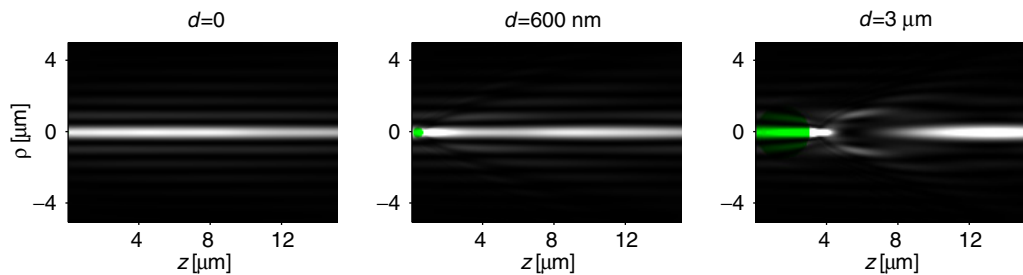


Figure 12. Side view of the BB self-reconstruction behind the polystyrene object placed at $z = 0\text{ }\mu\text{m}$. The surrounding medium is water and a single BB is considered with diameter of its core equal to $0.5\text{ }\mu\text{m}$. The left image shows an ideal BB without any object ($d = 0\text{ nm}$, left image), with the biggest object used in our experiments ($d = 600\text{ nm}$, middle) and with a polystyrene sphere with diameter $d = 3\text{ }\mu\text{m}$ (right). The green spot on the left indicates the size of the object.

5. More co-propagating BBs

We were interested in whether the object confinement improves for three and four interfering co-propagating beams. If the beams have the same on-axis intensities and their propagation constants satisfy

$$k_{z(j+1)} - k_{zj} = \Delta k = \text{const}, \quad (1)$$

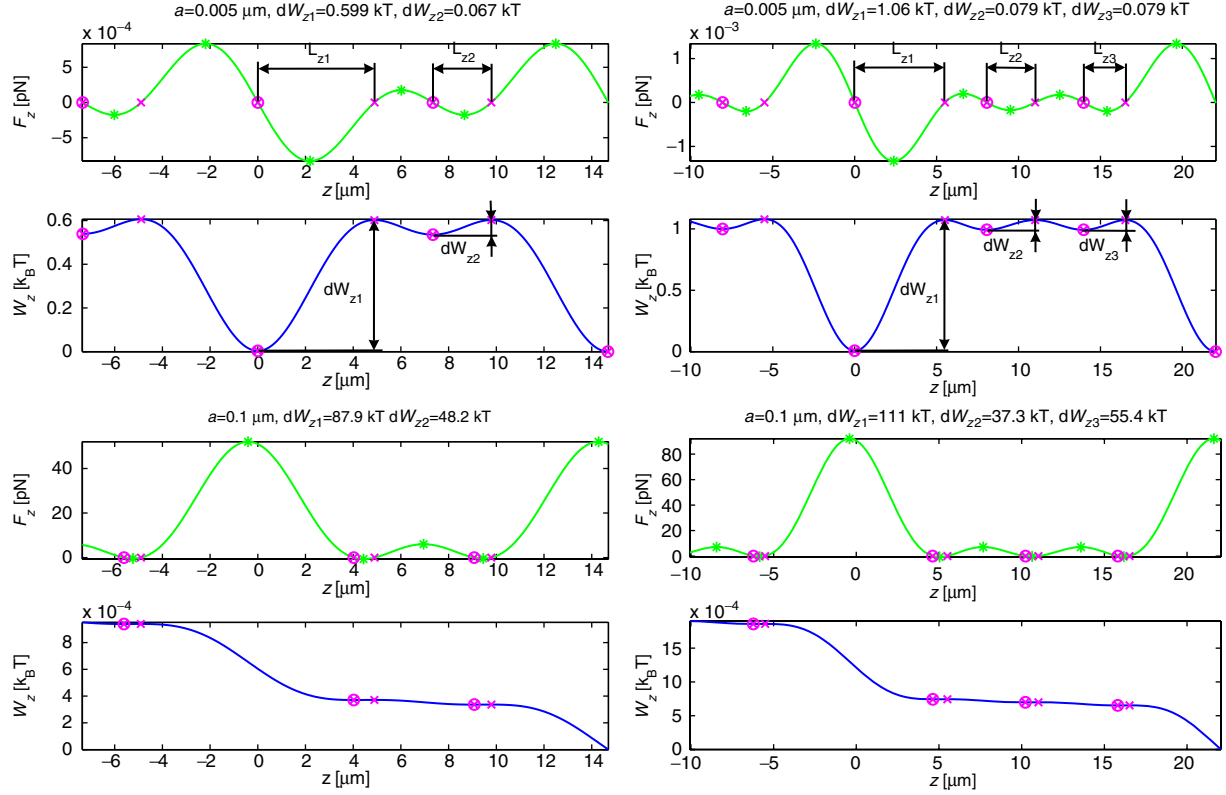


Figure 13. Left column: the longitudinal force (green) and longitudinal potential profile (blue, $W_z = -\int F_z dz$) for three co-propagating beams (see [movie 5](#)). The following beam widths and the powers in the central maximum of the BBs were assumed to satisfy the self-imaging conditions: $r_{\text{bes}1} = 0.437 \mu\text{m}$, $r_{\text{bes}2} = 0.575 \mu\text{m}$, $r_{\text{bes}3} = 1.156 \mu\text{m}$, $P_{\text{bes}1} = 0.323 \text{ W}$, $P_{\text{bes}2} = 0.560 \text{ W}$, $P_{\text{bes}3} = 2.263 \text{ W}$. Right column: the longitudinal force (green) and longitudinal potential profile obtained for four beams (see [movie 6](#)) and the following parameters: $r_{\text{bes}1} = 0.437 \mu\text{m}$, $r_{\text{bes}2} = 0.515 \mu\text{m}$, $r_{\text{bes}3} = 0.663 \mu\text{m}$, $r_{\text{bes}4} = 1.156 \mu\text{m}$, $P_{\text{bes}1} = 0.323 \text{ W}$, $P_{\text{bes}2} = 0.449 \text{ W}$, $P_{\text{bes}3} = 0.745 \text{ W}$, $P_{\text{bes}4} = 2.263 \text{ W}$. The equilibrium position is labelled by \otimes , non-equilibrium position by \times and forces extrema by $*$. We assumed the intensity of the electric field on the optical axis the same for both beams and it was equal to the electric field intensity of 1 W Gaussian beam with beam waist $1 \mu\text{m}$ ($E = 1.8 \times 10^{12} \text{ V m}^{-1}$).

they interfere constructively at the place of the maximum of the beam with the biggest propagation constant (k_{z3} for three beams and k_{z4} for four beams). We assumed that the bigger the beam index j the bigger the propagation constant of the beam k_{zj} . If we were not limited by the sizes of k_{zj} , the axial intensity maximum along the beam propagation would get narrower with increasing number of interfering beams. In this case, the gradient force would be stronger, too. Unfortunately, at the microscale, we are limited by the numerical apertures of the telescope lenses on one side and therefore we cannot create arbitrarily small k_{z1} . On the other hand, we put our restriction on the available laser power of the wider beams and we assume that the beams have to have the same

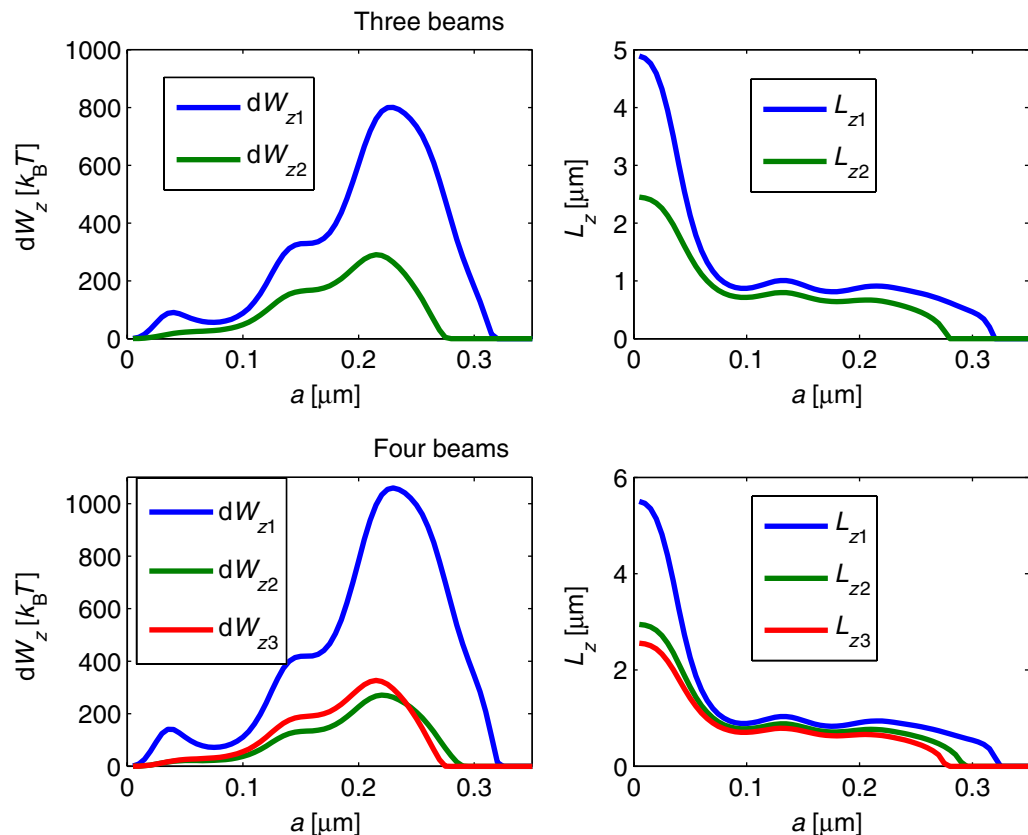


Figure 14. The axial depth of the optical trap dW_z and axial length of the trap L_z (defined in figure 13) for different radii of polystyrene spheres dispersed in water. The parameters of the beams were the same as in the previous figure. The radii of the cores of co-propagating BBs r_{bes1} and r_{bes2} were the same as in figure 1.

intensity of the electric field on the optical axis to interfere destructively here. This is an artificial restriction because a detailed study of the configurations with non-equal on-axis field intensities exceeds the limits of this paper. Moreover, wider beams (bigger k_{z3} or k_{z4}) also generate more heating in the sample cell.

In our experimental setup, we satisfied both limiting conditions and therefore the widths of the next extra beams have to be in between the two values mentioned above for two co-propagating beams. Taking into mind equation (1) we obtain for three co-propagating beams $r_{bes1} = 0.437 \mu m$, $r_{bes2} = 0.575 \mu m$, $r_{bes3} = 1.156 \mu m$ and in the case of four beams $r_{bes1} = 0.437 \mu m$, $r_{bes2} = 0.515 \mu m$, $r_{bes3} = 0.663 \mu m$, $r_{bes4} = 1.156 \mu m$. In this case the Talbot distance of repeating pattern will increase to $z_T = 14.85 \mu m$ and $z_T = 22.03 \mu m$ for three and four co-propagating beams, respectively.

Experimentally it is not possible to put the third or the fourth axicon into the setup without incurring huge losses of trapping power. Therefore, we only performed theoretical simulations using the same model described in the appendix. The results are shown in figures 13 and 14. It is seen that more longitudinal traps are created with different properties—length L_z and

depth dW_z (see figure 14). If the deepest trap (blue) is compared with the two-beam case in figure 2, we found the following.

- (i) The deepest trap is for bead radius $a = 0.23 \mu\text{m}$ for three and four beams comparing to $a = 0.22 \mu\text{m}$ for two beams.
- (ii) The more beams used, the deeper the trap: four beams: $dW_{z1}^{(4)} = 1060k_B T$; three beams: $dW_{z1}^{(3)} = 800k_B T$; two beams: $dW_{z1}^{(2)} = 649k_B T$. But if these values are normalized to the same intensity of the electric field at the maximum equal to two beams, we obtain: $dW_{z1}^{(4)} = dW_{z1}^{(4)} 4/16 = 265k_B T$; $dW_{z1}^{(3)} = dW_{z1}^{(3)} 4/9 = 356k_B T$; $dW_{z1}^{(2)} = 649k_B T$. It is immediately seen that the two-beam configuration is the most effective one with respect to the laser power demands.
- (iii) The more beams used, the bigger the particles that can be confined but the increase in bead size is not so dramatic: four beams: $a_{\text{max}} = 0.32 \mu\text{m}$; three beams: $a_{\text{max}} = 0.315 \mu\text{m}$; two beams: $a_{\text{max}} = 0.29 \mu\text{m}$.
- (iv) The trap length is very similar for majority of the particle radii $L_z \simeq 1 \mu\text{m}$. The more beams used, the longer the trap for tiny objects.
- (v) For three and four beams there exist shallower traps (full green, dashed red). Their maximal depths can be found for particles of similar radii as for the deepest trap. The maximal bead size that they can confine is smaller than that in the case of the deepest trap.

Therefore, under the studied conditions, we can assert that using more beams does not bring any significant improvement.

6. Conclusions

In this paper, we presented for the first time the theoretical description of how to calculate fast optical forces acting on dielectric objects placed into a vectorial BB behind the axicon. This model was applied to the case of two, three and four co-propagating beams of maximal and minimal radii of the core of the BB equal to 0.437 and $1.156 \mu\text{m}$, respectively. It was shown that in the studied configuration the axial depth of the optical trap increases and reaches its maximum for polystyrene beads of radii 220 – 230 nm. At the same time, it was shown for polystyrene particles that the work needed to free them radially can be much smaller and even reach zero. Under the studied conditions increasing the number of co-propagating beams does not dramatically change the size of the objects providing the deepest trap, nor the maximal bead radii that can be confined ($\simeq 300$ nm).

Experimentally, we focused on two co-propagating BBs of the same parameters as above and on the polystyrene objects of radii in the range 100 – 300 nm. Unfortunately, we did not succeed in particle confinement without fluid flow because of the large laser power requirement and the beam aberrations caused by the axicons used. Since the trap was not deep enough and did not have the same properties, the objects escaped radially from the trap. If we generated a fluid flow against the beam propagation, the objects were pushed closer to the intensity maximum where the trap in radial direction was deeper. In this arrangement we were able to confine all studied objects. They gradually self-organized into a 1D array with inter-bead spacing equal to $7.68 \mu\text{m}$. The whole structure was delivered by $250 \mu\text{m}$ if we employed the mechanism of optical conveyor belt and changed the phase of one of the co-propagating BBs. In the stationary

case (without the optical conveyor belt in action), we observed how the excitation caused by particle exchange in the trap propagates over the array. We focused on beads of radii 300 nm and we proved that the velocity of this excitation was equal to $620 \pm 80 \mu\text{m s}^{-1}$ even in seven subsequent events. This proves that the properties of the traps are very similar and the conditions of the experiment were stable.

The system described here has many unique properties that can be applied in other branches. If wider beams were used together with axicons having smaller aberrations the system would be rotationally symmetric around the propagation axis. Since the distance between optical traps in co-propagating beams is at least $20\times$ bigger than in the case of counter-propagating ones, the dynamics of stochastic motion and especially the problem of the first escape from the trap in periodic potential can be easily studied in two dimensions (longitudinal and lateral) without enormous demands on the stability of the system and resolution of the position detection. Due to this larger distance and the self-reconstructing property of the non-diffracting beams, significant interaction between confined objects starts only when the object leaves the trap and jumps to the trap of its neighbour. If a fast CCD camera is used, the interesting dynamics of this exchange and excitation spreading can be studied. The setup with co-propagating beams and the fluid counter-flow generates many optical traps with very similar properties. If wider beams are used, there will be bigger distance between neighbouring traps. Therefore, more objects can be analysed repeatedly if the principles of single beam optical chromatography [34] are applied.

Acknowledgments

This work was supported by the EC 6FP NEST ADVENTURE Activity (ATOM3D, project no 508952), ISI IRP (AV0Z20650511), MCT (FT-TA2/059).

Appendix A. Calculation of optical forces in BBs

A.1. Description of the field

We assume that an incident beam passing through an axicon creates an ideal BB. We are focused here on the BBs with narrow central core (comparable to the laser wavelength). Therefore, we developed a non-paraxial (vectorial) description of the problem. Inspired by Wolf [35] and Stamnes [36], we expressed the field behind the axicon using the spectrum of plane waves. Assuming the centre of coordinate system (x, y, z) at the apex of the axicon the following expressions are obtained for electric and magnetic fields:

$$\mathbf{E}(\mathbf{r}) \equiv \int_0^{2\pi} \mathbf{E}_{\text{PW}}(\alpha_0, \beta) e^{i\mathbf{k}\cdot\mathbf{r}} d\beta, \quad (\text{A.1})$$

$$\mathbf{B}(\mathbf{r}) \equiv \int_0^{2\pi} \mathbf{B}_{\text{PW}}(\alpha_0, \beta) e^{i\mathbf{k}\cdot\mathbf{r}} d\beta, \quad (\text{A.2})$$

where α_0 and β are the polar and azimuthal angles, respectively, with respect to the axicon and

$$\begin{aligned} \mathbf{E}_{\text{PW}}(\alpha_0, \beta) &\equiv E_{\text{PW}x}(\alpha_0, \beta)\mathbf{e}_x + E_{\text{PW}y}(\alpha_0, \beta)\mathbf{e}_y + E_{\text{PW}z}(\alpha_0, \beta)\mathbf{e}_z \\ &= E_{\text{PW}0}(\alpha_0, \beta) \left\{ [\cos \alpha_0 + \sin^2 \beta (1 - \cos \alpha_0)]\mathbf{e}_x \right. \\ &\quad \left. - [(1 - \cos \alpha_0) \sin \beta \cos \beta]\mathbf{e}_y + \sin \alpha_0 \cos \beta \mathbf{e}_z \right\}, \end{aligned} \quad (\text{A.3})$$

$$\begin{aligned}\mathbf{B}_{\text{PW}}(\alpha_0, \beta) &\equiv \frac{\mathbf{k}}{\omega} \times \mathbf{E}_{\text{PW}}(\alpha_0, \beta) \\ &= B_{\text{PW0}}(\alpha_0, \beta) \{ -[(1 - \cos \alpha_0) \sin \beta \cos \beta] \mathbf{e}_x \\ &\quad + [1 - \sin^2 \beta (1 - \cos \alpha_0)] \mathbf{e}_y + \sin \alpha_0 \sin \beta \mathbf{e}_z \},\end{aligned}\quad (\text{A.4})$$

where \mathbf{e}_j ($j = x, y, z$) are unit vectors of Cartesian coordinate system, ω is the field frequency, $E_{\text{PW}j}(\alpha_0, \beta)$ are the components of the electric field, $E_{\text{PW0}}(\alpha_0, \beta)$ the amplitude of component of the plane wave spectrum with wavevector direction made by polar angles α_0 and azimuthal angle β . If the problem is rotationally symmetric (no dependence on β), the integration in equations (A.1) and (A.2) can be performed and we get in a cylindrical system of coordinates (z, ρ, ϕ) for a BB propagating in the positive direction of the z -axis:

$$\mathbf{E}(\mathbf{r}) = E_{\text{B0}}(\alpha_0) e^{ik_z z} \{ [J_0(\sigma) + J_2(\sigma) P_{\perp} \cos(2\phi)] \mathbf{e}_x + J_2(\sigma) P_{\perp} \sin(2\phi) \mathbf{e}_y - i2J_1(\sigma) P_{\parallel} \cos \phi \mathbf{e}_z \}, \quad (\text{A.5})$$

$$\mathbf{B}(\mathbf{r}) = B_{\text{B0}}(\alpha_0) e^{ik_z z} \{ J_2(\sigma) P_{\perp} \sin(2\phi) \mathbf{e}_x + [J_0(\sigma) - J_2(\sigma) P_{\perp} \cos(2\phi)] \mathbf{e}_y - i2J_1(\sigma) P_{\parallel} \sin \phi \mathbf{e}_z \}, \quad (\text{A.6})$$

where E_{B0} is the on-axis electric field component of the BB, J_j is the Bessel function of j th order, \mathbf{k} the wavevector in the medium, \mathbf{e}_j ($j = x, y, z$) are unit vectors of Cartesian coordinate system, ρ and ϕ are radial coordinate and azimuthal angle in cylindrical system of coordinates, and

$$\rho = \sqrt{x^2 + y^2}, \quad \phi = \arctan \frac{y}{x}, \quad \sigma = k\rho \sin \alpha_0 = k_r \rho, \quad (\text{A.7})$$

$$P_{\perp} = \frac{1 - \cos \alpha_0}{1 + \cos \alpha_0}, \quad P_{\parallel} = \frac{\sin \alpha_0}{1 + \cos \alpha_0}, \quad P_{\perp}^2 = P_{\parallel}^2, \quad (\text{A.8})$$

$$E_{\text{B0}} = \pi E_{\text{PW0}}(\alpha_0) (1 + \cos \alpha_0), \quad B_{\text{B0}}(\alpha_0) = \frac{k}{\omega} E_{\text{B0}}(\alpha_0), \quad (\text{A.9})$$

$$k_z = k \cos \alpha_0. \quad (\text{A.10})$$

The time-averaged Poynting vector has the form

$$\mathbf{S} = \frac{1}{2\mu_0} \Re(\mathbf{E} \times \mathbf{B}^*) \quad (\text{A.11})$$

and substitution from equations (A.5) and (A.6) gives

$$S_z(\sigma) = E_{\text{B0}}^2(\alpha_0) \frac{k}{2\omega\mu_0} [J_0^2(\sigma) - J_2^2(\sigma) P_{\perp}^2], \quad S_x(\sigma) = 0, \quad S_y(\sigma) = 0. \quad (\text{A.12})$$

It is seen that the Poynting vector is completely symmetrical around the propagation axis even for the non-paraxial beam and as expected it does not depend on the longitudinal positions.

The width of the central core of the BB can be defined using equation (A.12) looking for $S_z = 0$. For simplicity, let us neglect the J_2 term and define the width of the central

core of the BB as

$$J_0(k \sin \alpha_0 r_{\text{bes}}) = 0 \Rightarrow r_{\text{bes}} = \frac{2.4048 \lambda_{\text{vac}}}{2\pi n \sin \alpha_0}, \quad (\text{A.13})$$

where λ_{vac} is the wavelength in the vacuum and n is the refractive index of the medium where the beam propagates. If the beam passes through the perpendicular boundary into a medium with different optical properties, the term $n \sin \alpha_0$ is constant and so the width of the BB stays the same.

The total power in the core of the BB is obtained by:

$$\begin{aligned} P_{\text{bes}} &= 2\pi \int_0^{r_{\text{bes}}} S_z(k\rho \sin \alpha_0) \rho d\rho \\ &= \frac{\pi E_{\text{B0}}^2 r_{\text{bes}}^2}{2\omega \mu_0 2.4048^2} J_1^2(2.4048) [2.4048^2 (1 - P_{\perp}^2) - 4P_{\perp}^2]. \end{aligned} \quad (\text{A.14})$$

Even in our case $P_{\perp}^2 \ll 0.0011$ and therefore it can be neglected:

$$P_{\text{bes}} \simeq \frac{\pi k E_{\text{B0}}^2 r_{\text{bes}}^2}{2\omega \mu_0} J_1^2(2.4048). \quad (\text{A.15})$$

A combination of several co-propagating or counter-propagating beams can be generally expressed as a sum of individual fields. In the non-paraxial case, the expressions are rather lengthy but let us show the final field distribution at the optical axis in the case of sum of N beams. From equation (A.5) for $\rho = 0$ we get:

$$\mathbf{E}(0, z) = \sum_{j=1}^N E_{\text{B0}}(\alpha_0^{(j)}) e^{ik_z^{(j)} z} = E_{\text{B0}}(\alpha_0^{(1)}) \sum_{j=1}^N e^{ik_z^{(j)} z}. \quad (\text{A.16})$$

If we assume $k_z^{(j+1)} - k_z^{(j)} = \Delta k_z = \text{const}$, we obtain

$$\mathbf{E}(0, z) = E_{\text{B0}}(\alpha_0^{(1)}) e^{ik_z^{(1)} z} \sum_{j=0}^{N-1} e^{ij\Delta k_z z} = E_{\text{B0}}(\alpha_0^{(1)}) e^{ik_z^{(1)} z} \frac{e^{iN\Delta k_z z} - 1}{e^{i\Delta k_z z} - 1}, \quad (\text{A.17})$$

$$S_z^{(N)}(0, z) = E_{\text{B0}}^2(\alpha_0^{(1)}) \frac{k}{2\omega \mu_0} \frac{1 - \cos(N\Delta k_z z)}{1 - \cos(\Delta k_z z)}, \quad (\text{A.18})$$

where by $S_z^{(N)}(0, z)$ we denoted the longitudinal component of the Poynting vector for N interfering beams. If $\Delta k_z^{(N)}$ is constant and does not depend on the number of interfering beams N , the peak is getting narrower and higher (see figure A.1(a)). But if $\Delta k_z^{(N)} = \Delta k_z^{(2)} / (N - 1)$ as considered in section 5, the peaks are wider and farther from each other with increasing N (see figure A.1(b)). The distance between neighbouring peaks is called the Talbot distance and is obtained by

$$z_T = \frac{2\pi}{\Delta k_z} = \frac{2\pi}{k_z^{(2)} - k_z^{(1)}} = \frac{\lambda_{\text{vac}}}{n(\cos \alpha_0^{(2)} - \cos \alpha_0^{(1)})}. \quad (\text{A.19})$$

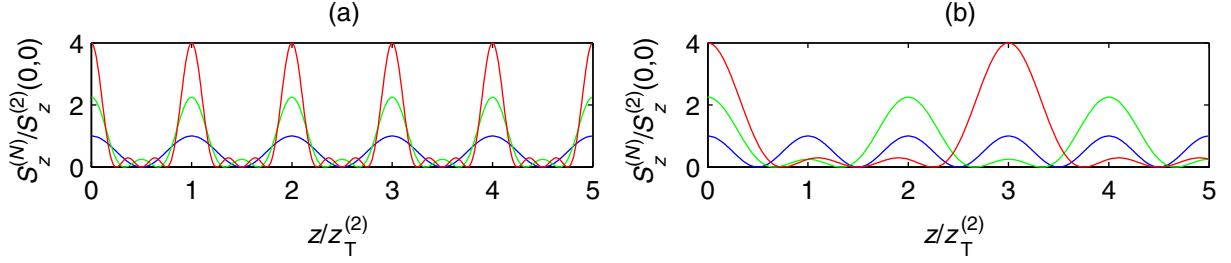


Figure A.1. Comparison of the maxima in the self-imaging if the Δk_z is constant with increasing number of beams N (a) and if the Δk_z changes as $\Delta k_z^{(N)} = \Delta k_z^{(2)}/(N-1)$ with increasing N (b). $z_T^{(2)}$ is the Talbot distance (spatial period of the maximal peak) for two interfering beams.

A.2. Calculation of optical forces for Mie particles

We used the Barton's method [26] to express the optical forces acting on spherical micro-particles placed into a single non-diffracting beam or into the interference field created by several non-diffracting beams. This method is based on the expansion of incident BB into a series of spherical harmonics with coefficients A_{lm} and B_{lm} done by:

$$A_{lm} = \frac{1}{l(l+1)\psi_l(\gamma)} \int_0^{2\pi} \int_0^\pi \sin \theta E_r^{(i)}(\mathbf{a} + \mathbf{r}_0) Y_{lm}^*(\theta, \varphi) d\theta d\varphi, \quad (\text{A.20})$$

$$B_{lm} = \frac{1}{l(l+1)\psi_l(\gamma)} \int_0^{2\pi} \int_0^\pi \sin \theta B_r^{(i)}(\mathbf{a} + \mathbf{r}_0) Y_{lm}^*(\theta, \varphi) d\theta d\varphi, \quad (\text{A.21})$$

where $\gamma = 2\pi a/\lambda$, \mathbf{a} is radius vector of the sphere, $E_r^{(i)}$ ($B_r^{(i)}$) is the radial component of the electric (magnetic) field incident on the sphere in spherical system of coordinates (a, θ, φ) having its beginning at the sphere centre, $\mathbf{r}_0 = (x_0, y_0, z_0)$ is the position vector of the sphere centre in the coordinate system of the beam.

If we used the fields derived above (equations (A.5) and (A.6)), the forces could be obtained from equations (A.20) and (A.21) if

$$E_r(\mathbf{r}_0 + \mathbf{a}) = E_x(\mathbf{r}_0 + \mathbf{a}) \sin \theta \cos \varphi + E_y(\mathbf{r}_0 + \mathbf{a}) \sin \theta \sin \varphi + E_z(\mathbf{r}_0 + \mathbf{a}) \cos \theta,$$

$$\begin{aligned} \mathbf{r}_0 + \mathbf{a} &= \rho \cos \phi \mathbf{e}_x + \rho \sin \phi \mathbf{e}_y + z \mathbf{e}_z \\ &= (x_0 + a \cos \varphi \sin \theta) \mathbf{e}_x + (y_0 + a \sin \varphi \sin \theta) \mathbf{e}_y + (z_0 + a \cos \theta) \mathbf{e}_z, \end{aligned}$$

$$\rho = \sqrt{x_0^2 + y_0^2 + a^2 \sin^2 \theta + 2a \sin \theta (x_0 \cos \varphi + y_0 \sin \varphi)},$$

$$\tan \phi = \frac{y_0 + a \sin \varphi \sin \theta}{x_0 + a \cos \varphi \sin \theta}.$$

This method is straightforward but quite lengthy for bigger objects because of double integration. Therefore, we derived a faster method using only single integration that employs the fact that the BB is a superposition of plane waves with delta distribution in polar angle $\simeq \delta(\alpha - \alpha_0)$. The

radial component of the field is obtained by

$$E_r(\mathbf{r}_0 + \mathbf{a}) = E_x(\mathbf{r}_0 + \mathbf{a}) \sin \theta \cos \varphi + E_y(\mathbf{r}_0 + \mathbf{a}) \sin \theta \sin \varphi + E_z(\mathbf{r}_0 + \mathbf{a}) \cos \theta. \quad (\text{A.22})$$

From equation (A.1) we get:

$$\mathbf{E}(\mathbf{r}_0 + \mathbf{a}) = \int_0^{2\pi} \mathbf{E}_{\text{PW}}(\alpha_0, \beta) e^{i\mathbf{k} \cdot (\mathbf{r}_0 + \mathbf{a})} d\beta. \quad (\text{A.23})$$

The expression $\exp[i\mathbf{k}(\alpha_0, \beta)\mathbf{r}_0]$ does not depend on the variables θ, φ and $\exp[i\mathbf{k}(\alpha_0, \beta)\mathbf{a}(\theta, \varphi)]$ can be rewritten using Legendre polynomials and the addition theorem for spherical harmonics (see [37], p 110 and 471):

$$e^{i\mathbf{k}(\alpha_0, \beta)\mathbf{a}(\theta, \varphi)} = \frac{4\pi}{\gamma} \sum_{p=0}^{\infty} i^p \psi_p(\gamma) \sum_{q=-p}^p Y_{pq}^*(\alpha_0, \beta + \pi) Y_{pq}(\theta, \varphi). \quad (\text{A.24})$$

After some algebra using the conditions of normalization and orthogonality for spherical harmonics and recurrence between Legendre polynomials we obtain:

$$\begin{aligned} A_{lm} = & \frac{1}{l(l+1)\psi_l(\gamma)} \frac{2\pi}{\gamma} \int_0^{2\pi} e^{i\mathbf{k}(\alpha_0, \beta)\mathbf{r}_0} \left\{ \left[i^{l-1} \psi_{l-1}(\gamma) Y_{l-1m}^*(\alpha_0, \beta + \pi) \sqrt{\frac{(l+m)(l-m)}{(2l-1)(2l+1)}} \right. \right. \\ & + i^{l+1} \psi_{l+1}(\gamma) Y_{l+1m}^*(\alpha_0, \beta + \pi) \sqrt{\frac{(l-m+1)(l+m+1)}{(2l+1)(2l+3)}} \left. \right] 2E_{\text{PW}z}(\alpha_0, \beta) \\ & + \left[i^{l+1} \psi_{l+1}(\gamma) Y_{l+1m-1}^*(\alpha_0, \beta + \pi) \sqrt{\frac{(l-m+2)(l-m+1)}{(2l+1)(2l+3)}} \right. \\ & - i^{l-1} \psi_{l-1}(\gamma) Y_{l-1m-1}^*(\alpha_0, \beta + \pi) \sqrt{\frac{(l+m)(l+m-1)}{(2l-1)(2l+1)}} \left. \right] \\ & \times [E_{\text{PW}x}(\alpha_0, \beta) - iE_{\text{PW}y}(\alpha_0, \beta)] \\ & + \left[i^{l-1} \psi_{l-1}(\gamma) Y_{l-1m+1}^*(\alpha_0, \beta + \pi) \sqrt{\frac{(l-m)(l-m-1)}{(2l+1)(2l-1)}} \right. \\ & - i^{l+1} \psi_{l+1}(\gamma) Y_{l+1m+1}^*(\alpha_0, \beta + \pi) \sqrt{\frac{(l+m+1)(l+m+2)}{(2l+1)(2l+3)}} \left. \right] \\ & \times [E_{\text{PW}x}(\alpha_0, \beta) + iE_{\text{PW}y}(\alpha_0, \beta)] \left. \right\} d\beta. \quad (\text{A.25}) \end{aligned}$$

B_{lm} is obtained by exactly the same formula, except components of vector \mathbf{E} must be exchanged by components of vector \mathbf{B} .

References

- [1] Durnin J, Miceli J J and Eberly J 1987 Diffraction-free beams *Phys. Rev. Lett.* **58** 1449–1501
- [2] Gutiérrez-Vega J, Iturbe-Castillo M and Cháavez-Cerda S 2000 Alternative formulation for invariant optical fields: Mathieu beams *Opt. Lett.* **25** 1493–5

- [3] Bouchal Z and Olivík M 1995 Non-diffractive vector Bessel beams *J. Mod. Opt.* **42** 1555–66
- [4] Piestun R and Shamir J 1998 Generalized propagation-invariant wave fields *J. Opt. Soc. Am. A* **15** 3039–34
- [5] Tervo J, Vahimaa P and Turunen J 2002 On propagation-invariant and self-imaging intensity distribution of electromagnetic fields *J. Mod. Opt.* **49** 1537–43
- [6] Rayleigh L 1881 On copying diffraction-gratings, and on some phenomena connected therewith *Phil. Mag.* **11** 196–205
- [7] Bouchal Z, Horák R and Wagner J 1996 Propagation-invariant electromagnetic fields: theory and experiment *J. Mod. Opt.* **43** 1905–20
- [8] Chávez-Cerda S, Meneses-Nava M A and Hickmann J M 1998 Interference of traveling nondiffracting beams *Opt. Lett.* **23** 1871–3
- [9] Bouchal Z and Kyvalský J 2004 Controllable 3d spatial localization of light fields synthesized by non-diffracting modes *J. Mod. Opt.* **51** 157–76
- [10] Saastamoinen T, Tervo J, Vahimaa P and Turunen J 2004 Exact self-imaging of transversely periodic fields *J. Opt. Soc. Am. A* **21** 1424–9
- [11] Tervo J and Turunen J 2001 Rotating scale-invariant electromagnetic fields *Opt. Express* **9** 9–15
- [12] Zamboni-Rached M 2004 Stationary optical wave fields with arbitrary longitudinal shape by superposing equal frequency bessel beams: frozen waves *Opt. Express* **12** 4001–6
- [13] Garcés-Chávez V, McGloin D, Melville H, Sibbett W and Dholakia K 2002 Simultaneous micromanipulation in multiple planes using a self-reconstructing light beam *Nature* **419** 145–7
- [14] Ahluwalia B P S, Yuan X-C, Tao S H, Bu J, Wang H, Peng X and Niu H B 2005 Microfabricated-composite-hologram-enabled multiple channel longitudinal optical guiding of microparticles in nondiffracting core of a bessel beam array *Appl. Phys. Lett.* **87** 084104
- [15] Garcés-Chávez V, Roskey D, Summers M D, Melville H, McGloin D, Wright E M and Dholakia K 2004 Optical levitation in a bessel light beam *Appl. Phys. Lett.* **8** 4001–3
- [16] Čižmár T, Garcés-Chávez V, Dholakia K and Zemánek P 2005 Optical conveyor belt for delivery of submicron objects *Appl. Phys. Lett.* **86** 174101-1–174101-3
- [17] Zemánek P and Foot C J 1998 Atomic dipole trap formed by a blue detuned strong Gaussian standing wave *Opt. Commun.* **146** 119–23
- [18] Freearge T and Dholakia K 2002 Cavity-enhanced optical bottle beam as a mechanical amplifier *Phys. Rev. A* **66** 013413
- [19] Arlt J and Padgett M J 2000 Generation of a beam with a dark focus surrounded by regions of higher intensity: the optical bottle beam *Opt. Lett.* **25** 191–3
- [20] McGloin D, Spalding G C, Melville H, Sibbett W and Dholakia K 2003 Three-dimensional arrays of optical bottle beams *Opt. Commun.* **225** 215–22
- [21] Chen C-H, Tai P-T and Hsieh W-F 2004 Bottle beam from a bare laser for single-beam trapping *Appl. Opt.* **43** 6001–6
- [22] Ahluwalia B P S, Yuan X-C and Tao S H 2004 Generation of self-imaged optical bottle beams *Opt. Commun.* **238** 177–84
- [23] Ahluwalia B P S, Yuan X-C and Tao S H 2004 Transfer of ‘pure’ on-axis spin angular momentum to the absorptive particle using self-imaged bottle beam optical tweezers system *Opt. Express* **12** 5172–7
- [24] Dennis M R 2003 Braided nodal lines in wave superposition *New J. Phys.* **5** 134
- [25] Schonbrun E, Piestun R, Jordan P, Cooper J, Wulff K D, Courtial J and Padgett M 2005 3D interferometric optical tweezers using a single spatial light modulator *Opt. Express* **13** 3777–86
- [26] Barton J P, Alexander D R and Schaub S A 1989 Theoretical determination of net radiation force and torque for a spherical particle illuminated by a focused laser beam *J. Appl. Phys.* **66** 4594–602
- [27] Gardiner C W 2004 *Handbook of Stochastic Methods* (Berlin: Springer)
- [28] Risken H 1996 *The Fokker-Planck Equation* (Berlin: Springer)
- [29] Tatarkova S A, Sibbett W and Dholakia K 2003 Brownian particle in an optical potential of the washboard type *Phys. Rev. Lett.* **91** 038101

- [30] Cheezum M K, Walker W F and Guilford W H 2001 Quantitative comparison of algorithms for tracking single fluorescent particles *Biophys. J.* **81** 2378–88
- [31] Bouchal Z, Wagner J and Chlup M 1998 Self-reconstruction of a distorted nondiffracting beam *Opt. Commun.* **151** 207–11
- [32] Dholakia K, Little H, Brown C T A, Agate B, McGloin D, Paterson L and Sibbett W 2004 Imaging in optical micromanipulation using two-photon excitation *New J. Phys.* **6** 136
- [33] Goodman J W 1968 *Introduction to Fourier Optics* (New York: McGraw-Hill)
- [34] Hart S J and Terray A V 2003 Refractive-index-driven separation of colloidal polymer particles using optical chromography *Appl. Phys. Lett.* **83** 5316–8
- [35] Wolf E 1959 Electromagnetic diffraction in optical systems I. An integral representation of the image field *Proc. R. Soc. A* **253** 349–57
- [36] Stamnes J J 1986 *Waves in Focal Regions* (Bristol: Institute of Physics Publishing)
- [37] Jackson J D 1999 *Classical Electrodynamics* (New York: Wiley)